Observations of Upper-Tropospheric Temperature Inversions in the Indian Monsoon and Their Links to Convectively Forced Quasi-Stationary Kelvin Waves

RICHARD NEWTON AND WILLIAM RANDEL

National Center for Atmospheric Research, Boulder, Colorado

ABSTRACT

High-vertical-resolution temperature measurements from GPS radio occultation data show frequent upper-tropospheric inversions over the equatorial Indian Ocean during the summer monsoon season. Each year, around 30% of profiles in this region have temperature inversions near 15 km during the monsoon season, peaking during July–September. This work describes the space–time behavior of these inversions, and their links to transient deep convection. The Indian Ocean inversions occur episodically several times each summer, with a time scale of 1–2 weeks, and are quasi stationary or slowly eastward moving. Strong inversions are characterized by cold anomalies in the upper-troposphere (12–15 km), warm anomalies in the tropopause layer (16–18 km), and strong zonal wind anomalies that are coherent with temperature anomalies. Temperature and wind anomalies are centered over the equator and show a characteristic eastward phase tilt with height with a vertical wavelength near 5 km, consistent with a Kelvin wave structure. Composites of outgoing longwave radiation (OLR) show that strong inversions are linked to enhanced deep convection over the equatorial Indian Ocean, preceding the inversions by ∼2–6 days. These characteristics suggest that the inversions are linked to convectively forced Kelvin waves, which are Doppler shifted by the easterly monsoonal winds such that they remain quasi stationary in the equatorial Indian Ocean. These large-scale waves influence circulation on the equatorial side of the Indian monsoon anticyclone; they may provide a positive feedback to the underlying convection, and are possibly linked with regions of shear-induced turbulence.

1. Introduction

In the tropics, temperatures typically decrease with height from the surface to a minimum in the tropical tropopause, near 16 km. This structure can be interrupted by narrow-scale local temperature increases with height, which are termed inversions. Temperature inversions occur in a variety of situations throughout the troposphere, often related to convection and/or the finescale structure of water vapor. Tropical inversions are often observed at the top of the boundary layer (∼1–2 km) associated with large-scale subsidence, and also near the 0°C level (∼4 km), likely tied to melting within precipitation systems (Johnson et al. 1996). Layered structures in the water vapor (and ozone) are often observed in the tropical troposphere (Newell et al. 1999), and inversions can be found linked to strong water vapor gradients (Mapes and Zuidema 1996). In general, inversions act as a barrier to vertical transport and can influence the development of convection.

Inversions are also observed in the tropical mid- and upper troposphere. Fujiwara et al. (2003a) documented narrow inversion layers over ∼12–14 km over the equatorial eastern Pacific Ocean, associated with strong vertical gradients in water vapor and associated longwave cooling at the bottom of the inversions. Biondi et al. (2012) found strong inversions at the top of intense convective systems (∼12–16 km), likely also related to strong water vapor gradients, and Biondi et al. (2013) found the same behavior for tropical cyclones. Frequent temperature inversions are also observed around the subtropical jet, where the extratropical tropopause and the tropical tropopause occur simultaneously in the same vertical profiles at around 10 and 16 km, respectively (so-called double tropopause events; e.g., Randel et al. 2007). However, this situation is distinct from inversions in the deep tropics, which are the focus of this study. Nishi et al. (2010) noted the frequent occurrence of upper-tropospheric temperature inversions over the equatorial Indian Ocean in the boreal summer monsoon season, based on GPS radio occultation measurements. Nishi et al. (2010) suggests that

the inversion layers result from a combination of Kelvin waves and Rossby waves forced by asymmetric heating in the Indian monsoon. The frequent occurrence of anomalous tropopause structure in this region was also highlighted by Nishimoto and Shiotani (2012).

Our work here is focused on further analysis of the boreal summer upper-tropospheric inversions using a variety of observational and reanalysis datasets. We derive a climatology of inversions from a long record (2001–17) of GPS radio occultation data, demonstrating the frequent occurrence of events over the Indian Ocean during the monsoon season (as shown by Nishi et al. 2010). Our work complements their analysis, which analyzed one year (2007), by using many years of data, and we examine the space–time structure of strong inversion events in temperatures and winds, and identify links to transient deep convection [using outgoing longwave radiation (OLR) as a proxy]. The observed characteristics are consistent with a large-scale equatorial Kelvin wave excited by transient convection, and we explore the coupling with the background flow that explains the waves' quasi-stationary behavior.

2. Data and analyses

a. GPS and meteorological data

We analyze temperature profiles from GPS radio occultation measurements covering 2001–17. GPS data have the attributes of high quality and high vertical resolution, with near-global sampling. We include data from seven individual satellites [or constellations, in the case of Constellation Observing System for Meteorology, Ionosphere and Climate (COSMIC)], including

- *Challenging Minisatellite Payload* (*CHAMP*; 19 May 2001–5 October 2008; Wickert et al. 2001),
- COSMIC (data from 22 April 2006–present; Anthes et al. 2008),
- Gravity Recovery and Climate Experiment (GRACE; 28 February 2007–30 November 2017; Beyerle et al. 2005),
- *MetOp-A* (1 October 2007–present; von Engeln et al. 2011) and *MetOp-B* (1 February 2013–present; von Engeln et al. 2011),
- Satellite de Aplicaciones Cientificas-C (*SAC-C*; 9 March 2006–3 August 2011; Hajj et al. 2004), and
- *TerraSAR-X* (10 February 2008–present; Beyerle et al. 2011).

The combination of data provides approximately 600 occultations per day (after 2006) over tropical latitudes 30°N–30°S (the focus of this work), equally distributed in longitude. The datasets were retrieved from the COSMIC

Data Analysis and Archive Center (CDAAC; http://cdaac-www.cosmic.ucar.edu/cdaac/index.html). The sampling density varies as a result of the availability of the various satellite missions that provide GPS radio occultation measurements; prior to 2006 the measurements were sparse, but increased by a factor of 20 in 2007–08 when COSMIC, GRACE, *MetOp-A* and *TerraSAR-X* were all newly in operation, with the number of profiles slowly decreasing after that as the satellites gradually degrade over time. We therefore use only the period 2007–17 for the composite analysis in this study (section 3c, for which dense data sampling is required).

The GPS radio occultation technique uses the refractivity of the GPS signal N:

$$N = \frac{77.66p}{T} + \frac{3.73 \times 10^5 e}{T^2} - \frac{4.03 \times 10^7 n_e}{f^2}, \quad (1)$$

where p is atmospheric pressure (hPa), T is temperature (K), e is water vapor pressure (hPa), n_e is the electron density (m^{-3}), and f is the frequency of the GPS radio signal (Hz). We use the dry profile retrievals (AtmPrf) in this study, which assumes the water vapor pressure and electron density effects on the refractivity are negligible. We analyze the GPS temperatures at a vertical spacing of 200 m, but acknowledge that this is oversampled compared to the vertical resolution of ~1 km. Since the features we are analyzing have vertical scales of several kilometers this does not impact the results. Identification of temperature inversions and their climatological characteristics are discussed below, and the GPS temperatures were gridded onto a $5° \times 5° \times 0.5$ km longitude–latitude–altitude grid by taking the mean temperatures of all data points that belong in each grid point. Likewise, the inversion statistics were calculated on the same grid by counting the number of profiles with and without inversions in each grid point. We also analyze meteorological variables derived from ERA-Interim (Dee et al. 2011) for the same time period as the GPS dataset (2001–17), retrieved from the UCAR Research Data Archive (RDA; https://rda.ucar.edu). This dataset is 6-hourly with a longitude–latitude resolution of ~0.75°, with data output on 37 pressure levels with a vertical resolution of ~1.2 km in the upper troposphere–lower stratosphere (UTLS). We subsample the ERA-Interim data into daily means on a $5° \times 5°$ longitude–latitude grid, to directly match the gridded GPS data.

We also evaluated gridded daily measurements of OLR as a proxy for deep convection, using the NOAA Interpolated Outgoing Longwave Radiation product daily mean data (Liebmann and Smith 1996). The OLR data are also gridded into daily means onto a $5° \times 5°$ longitude–latitude grid.

b. Identifying upper-tropospheric temperature inversions

As a background for our analyses, we examine the climatological occurrence of upper-tropospheric inversions from the long record of GPS data, defined as parts of a profile that have $dT/dz > 0$, and have $dT/dz < 0$ above and below the inversion, within the troposphere. We aim to objectively identify tropospheric inversions from GPS temperature profiles, such as the two examples shown in Fig. 1. One simple method is to take each individual profile, calculate the lapse-rate tropopause (LRT), and then search for inversions below that level. This is a straightforward calculation that produces climatological results similar to those shown below, except that it substantially undercounts the occurrence frequency in cases of large amplitude inversions [such as shown for profile (a) in Fig. 1]. In these cases, the bottom of the large inversion is identified as the tropopause, and hence not counted as an inversion.

An alternative approach is to identify inversions with respect to the long-term local climatological tropopause. For example, Fig. 1 shows the climatological summer temperature structure over the equatorial Indian Ocean, with an LRT at 16.6 km. In Fig. 1, the strong inversion near 15 km in profile (a) is now identified as an inversion, whereas it was not counted in the prior calculation. This behavior occurs frequently in the Indian Ocean region during boreal summer, so that the number of inversions is approximately doubled using the climatological tropopause criterion. We calculate a monthly climatological LRT dataset on a $5° \times 5°$ grid from the long-term GPS data, and our results are similar to those in, e.g., Schmidt et al. (2005) and Munchak and Pan (2014). Then, for each profile, we query which $5° \times 5°$ grid box and month the profile belongs in, look up the altitude of the climatological tropopause for this grid box and month, and search for inversions below this altitude. The resulting occurrence frequency statistics are then gridded onto a $5° \times 5°$ grid.

c. Global upper-troposphere inversion climatology

The monthly distribution of temperature inversions at 15 km is shown in Fig. 2, and note that results are only shown where the climatological tropopause is above 15 km, i.e., the deep tropics. In this, and the following analyses, 15 km inversions refer to inversions that have a positive temperature gradient between 15.0 and 15.5 km, and the results at 15 km refers to the average statistics of such inversions. The broadscale distribution in Fig. 2 shows a background of ~5% occurrence frequency throughout the tropics, with several regions of locally enhanced occurrence frequencies up to ~40%. Three regions
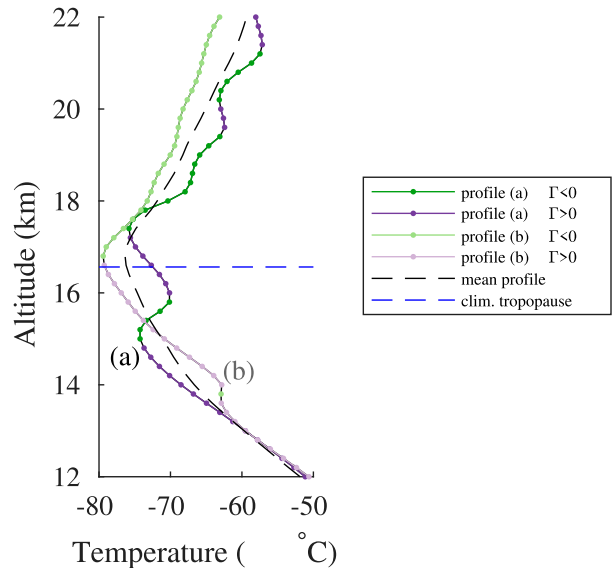

FIG. 1. Two example profiles, the first (a) is from 2000 UTC 9 Jul 2013, which has a large temperature inversion at 15–16 km, and the second (b) is from 1300 UTC 27 Sep 2013, which has a small temperature inversion at 14 km. A climatological profile taken from all the COSMIC profiles in the 5°S–0°, 60°–65°E grid box from 1 Jul–30 Sep 2013 is shown as a black dashed line, and the corresponding tropopause is shown as a horizontal blue dashed line.

can be highlighted that have a high proportion of 15 km temperature inversions in Fig. 2: the equatorial Indian Ocean between June and September (during the monsoon season), northern subtropical Africa in October–December, and Cuba and the surrounding Atlantic Ocean in June–July. In general, there is enhanced occurrence frequency of inversions on the edges of the tropics during much of the year; these inversions are linked to the occurrence of double tropopauses in the subtropics (e.g., Randel et al. 2007). Our further analyses focus on inversions over the equatorial Indian Ocean, which has the most prolonged period and most widespread region of frequent occurrences of temperature inversions.

3. Boreal summer inversions over the Indian Ocean

This section analyzes the statistical characteristics and variability of temperature inversions in the Indian monsoon region, and their links to large-scale meteorological structure and deep convection via composite analyses.

a. Spatial and temporal characteristics

The climatological spatial distribution of temperature inversions at 15 km for July–September in the Indian monsoon region is shown in Fig. 3. The number of
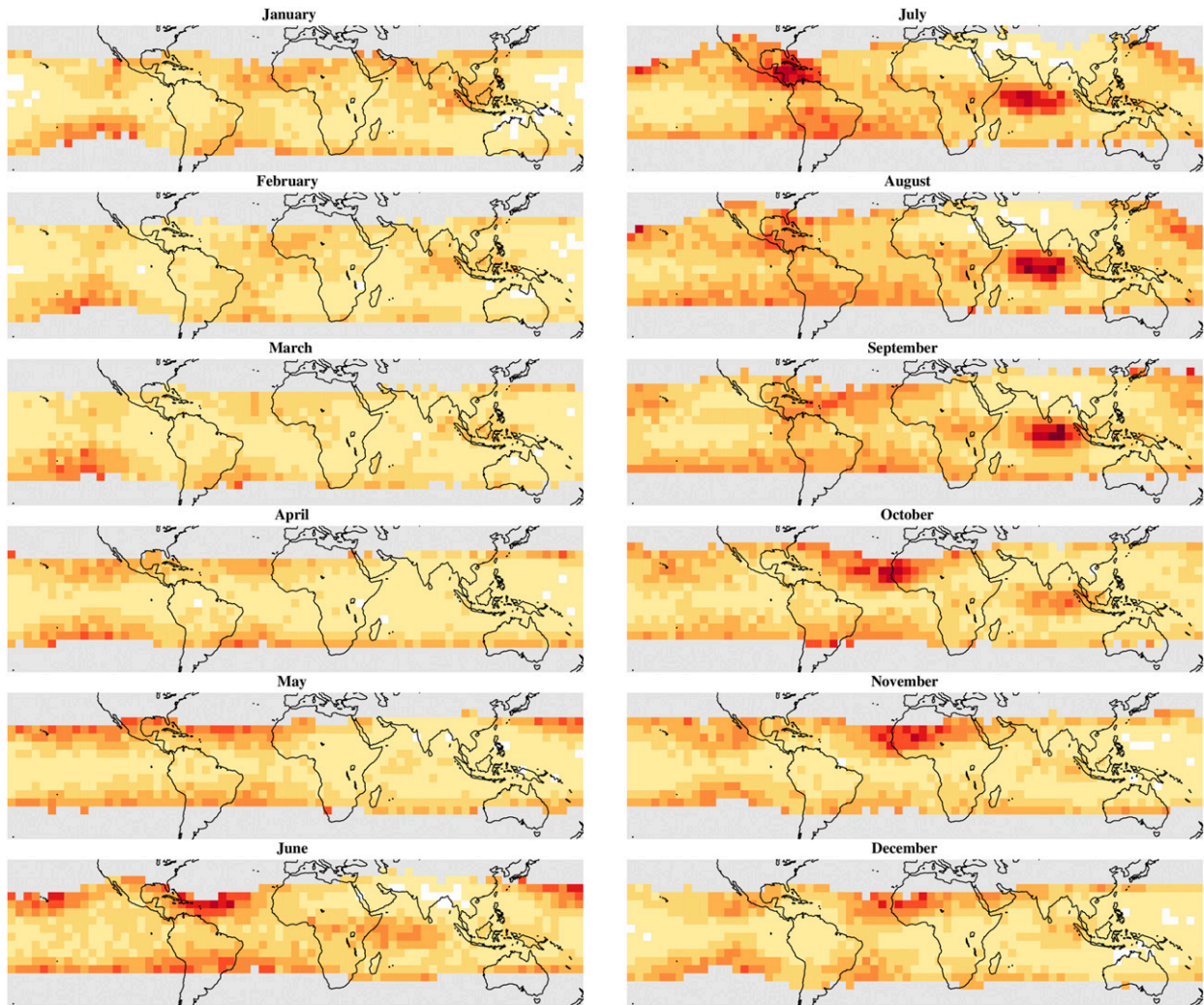
FIG. 2. Monthly climatology of tropical temperature inversions at 15 km from GPS data over 2001–17. Areas of most frequent temperature inversions are observed over the Indian Ocean during July–September, in northern Africa during October–December, and over Cuba and its surroundings during June–July.

profiles in each $5° \times 5°$ grid box is around 200–300 for each calendar month over the 18-yr period (an average of around 30 month^{-1} yr^{-1} after the launch of COSMIC in 2006). The highest frequency of inversions is ~20%–40% in Fig. 3, centered approximately over the equator (~10°N–10°S) for longitudes ~50°–90°E. The values obtained by these climatologies compare well with those obtained by Nishi et al. (2010) for the year 2007.

Time series of the occurrence frequency of inversions at 15 km averaged over the maximum region (10°N–10°S, 50°–90°E) are shown in Fig. 4 for 2009, and the statistics of 2007–17, based on daily data smoothed slightly in time. In 2009, and indeed in all years, there is a maximum occurrence of inversions from July to September, and the time series show episodic enhancements of inversions with a time scale of 1–2 weeks. For the whole region of interest, around 30% of profiles have a temperature inversion during boreal summer. There are also occasional enhancements of inversions up to 30% during January–March of some individual years. The frequency of occurrence of inversions as functions of altitude, latitude and longitude are shown in Fig. 5. Tropical inversions are found at altitudes down to ~13 km, and increase in frequency up to the climatological tropopause. The most frequent inversions are centered on the equator (Fig. 5a), with an upward- and eastward-sloping structure in longitude (Fig. 5b). These patterns are similar to the statistics shown in Nishi et al. (2010) for one year (2007). The largest proportion of temperature inversions are found at ~15 km, so subsequent analyses focus on the temperature inversions at 15 km.
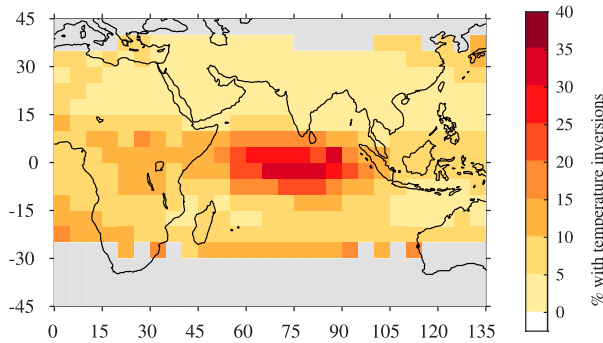
FIG. 3. Frequency of GPS radio occultation profiles with temperature inversions at 15 km during July–September. A gray box indicates that the altitude of this grid box is above the climatological tropopause.

FIG. 4. Smoothed 1-day average occurrence frequency for tropospheric temperature inversions at 15 km in the Indian monsoon region (10°S–10°N, 50°–90°E) for 2009 (black line), the mean of 2007–17 (solid magenta line) and the one standard deviation envelope of yearly values (dashed magenta lines). Most tropospheric temperature inversions occur between June and September, coincident with the monsoon season.

The frequent inversions in this region can influence the altitude of the LRT, as large inversions can be identified with a tropopause near 15 km. Figure 6 shows the distribution of LRT altitude for this region, revealing a wide distribution of altitudes covering ~14.5–17.5 km (with a mean near 16.2 km). The inversions near 15 km can often be classified as an LRT, explaining the wide low-altitude tail of the distribution in Fig. 6. These statistics are reflected in the relatively low-altitude average tropopause height in this area compared to surrounding regions, as noted in Munchak and Pan (2014). Occasionally ~15 km LRT are associated with a secondary (double) tropopause (Fig. 6), but this is a relatively rare occurrence found in 10% of all profiles.

b. Variability during 2009

We analyze variability during an individual year—2009—which was selected because it has multiple episodes of distinct temperature inversions, but similar behavior is found each year. Figure 7 shows the longitude-versus-time distribution of inversions over the equator (5°N–5°S), with several individual episodes of inversions lasting ~1–2 weeks (as seen in Fig. 4). In 2009, and also in other years, there is often a slow drift of the temperature inversions eastward over time. The temperature inversions occur predominantly along the equator; the inversions do not vary meridionally over time. Examples of temperature profiles with and without temperature inversions at 15 km during July 2009 are shown in Fig. 8, highlighting the distinct vertical structure.

The ERA-Interim data show that the inversions are also closely linked with variations in zonal winds in the upper troposphere. Figure 9 shows the zonal wind speed over the equator at 125 hPa (14.6 km) during 2009, highlighting acceleration of easterly winds in concert with occurrence of inversions. These equatorial easterly
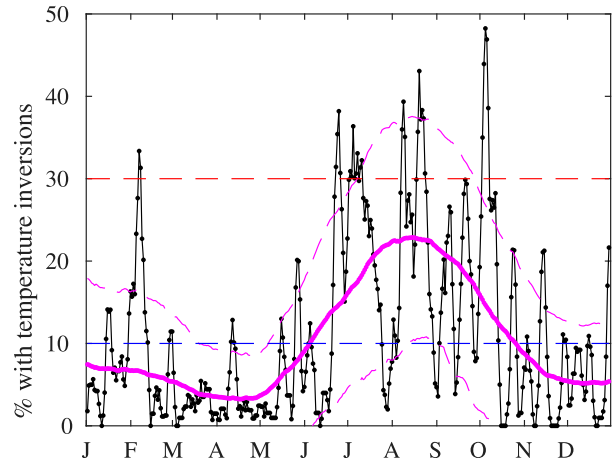
winds are part of the large-scale Indian monsoon anticyclone circulation (e.g., Hoskins and Rodwell 1995), and the results in Fig. 9 demonstrate that the inversions are tied to strong modulations of this circulation, as shown further below.

c. Composites of strong inversion events

Here we examine the composited temperature and wind structure for strong inversion events, using data over years 2007–17 (the period of dense GPS data). Composite analysis was performed by taking time series of daily 15 km inversion frequency, as shown in Fig. 4, and selecting the times that have the highest and lowest values (above 30% and below 10%). We then composite GPS temperatures, ERA-Interim winds, and OLR fields for the high-frequency and low-frequency inversion events, and calculate differences. This analysis also includes time-lag behavior among the different variables.

The height-versus-longitude structure of temperature anomalies over the equator associated with 15 km inversions is shown in Fig. 10a. The distinct patterns show warm anomalies above and cold anomalies below ~15 km, with an eastward phase tilt with height similar to the inversion frequency in Fig. 5a (the inversions occur between the cold and warm anomalies). Average anomaly amplitudes are of order ±4 K. The temperature anomalies are centered over the equator, and time evolution shows quasi-stationary or slow eastward propagation of the patterns over time (results not shown). Composite anomalies of zonal winds associated with 15 km inversions are shown in Fig. 10b, and note the
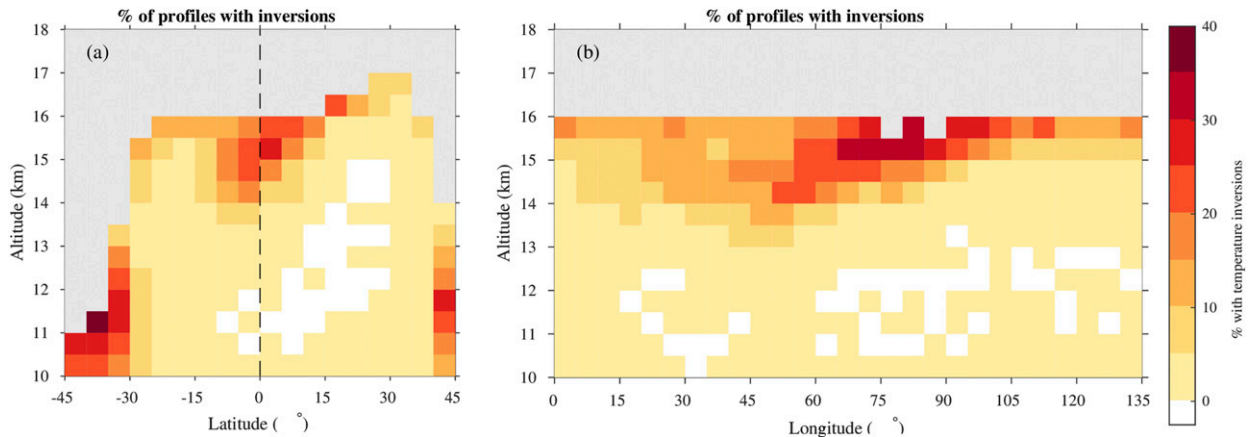
FIG. 5. Occurrence frequency of temperature inversions for July–September in the Indian monsoon region as a function of (a) latitude at 65°E and (b) longitude at the equator.

lower vertical resolution compared to the GPS temperatures. Zonal wind anomalies are characterized by patterns that are approximately in phase, or shifted slightly eastward compared to the temperatures in Fig. 10a (low temperatures and easterly winds at 14 km, and vice versa at 17 km); the exact phasing is difficult to quantify because of the different vertical resolutions of the data. Both temperatures and winds exhibit an eastward phase tilt with height with a vertical wavelength near 5 km. Strong easterly wind anomalies near 14 km ($\sim$10 m s^{-1}) reflect the correlation with inversions seen in Fig. 9. There are additional positive wind anomalies over $\sim$12–14 km, 110°–160°E that are not observed in temperatures.

Horizontal structure of the temperature and wind anomaly composites are shown in Fig. 11, for altitudes of 14.5 and 17 km. Anomalies at both levels are centered over the equator, approximately in phase between
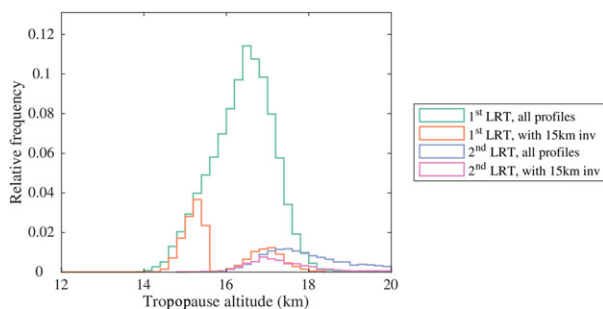
temperature and winds. As noted above, these wind anomalies (tied to inversion events) modulate the circulation in the southern part of the Indian monsoon anticyclone. The overall characteristics of winds and temperatures, including equatorially centered structure, eastward phase tilt with height, and coherent behavior of temperatures and zonal winds are suggestive of equatorial Kelvin waves (e.g., Wallace and Kousky 1968), although observations typically show that UTLS Kelvin

FIG. 6. Probability distribution function of lapse-rate tropopause altitudes over 10°S–10°N, 50°–90°E during July–September, including those with double tropopauses. The profiles with a 15 km inversion display a bimodal distribution of tropopauses, at 14–16 km and at 16–18 km, corresponding to strong and weak inversions, respectively. Infrequent double tropopauses also occur in this region.
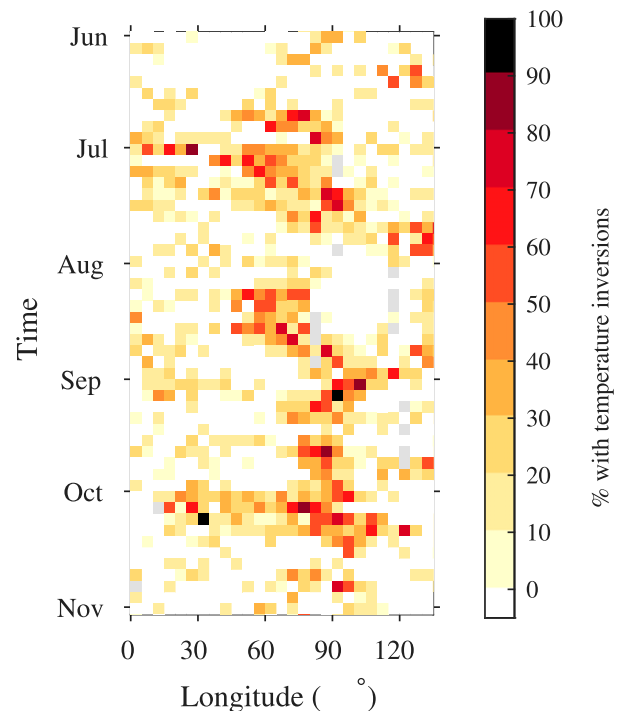

FIG. 7. Occurrence of temperature inversions over the equatorial Indian Ocean at 15 km as a function of longitude and time for 2009. The results are based on 3-day mean statistics over 5°S–5°N.
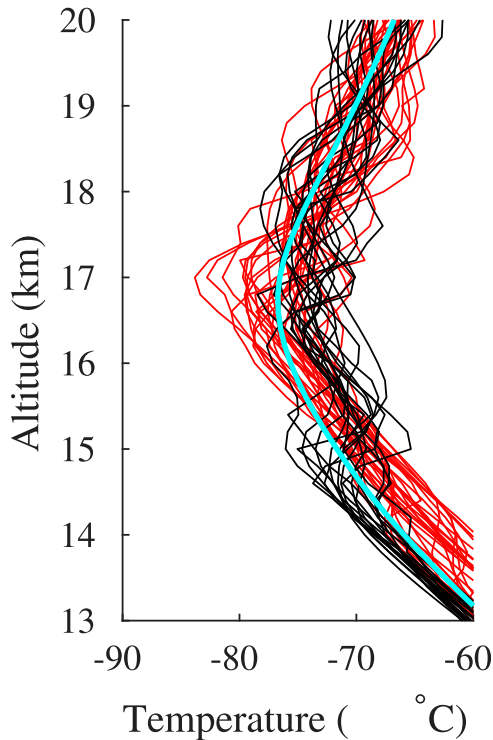
FIG. 8. Example GPS radio occultation profiles from July 2009 over 5°S–0°, 60°–65°E, showing events with 15 km inversions (black) and those without (red). The light blue line is the climatological profile of July–September, which has a tropopause near 16.2 km.
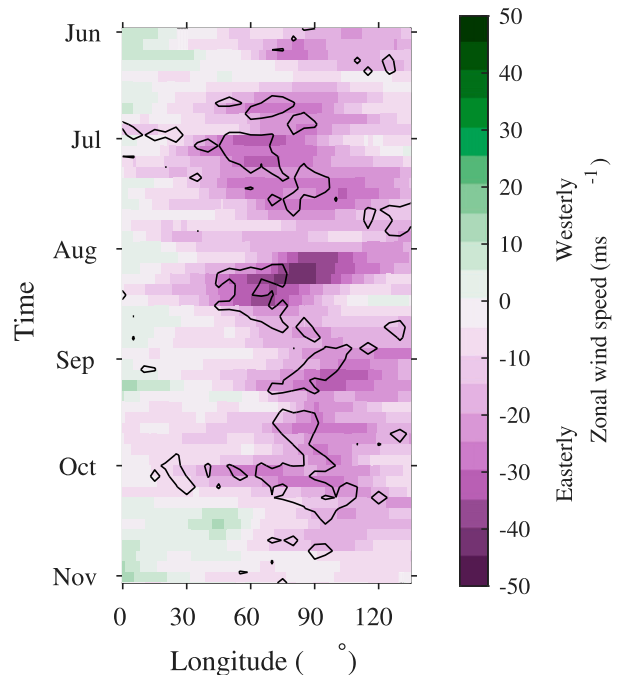

FIG. 9. Longitude–time distribution of zonal wind speed over the equator at 125 hPa (14.6 km) during summer 2009. The black contours enclose areas that have >30% of profiles with temperature inversions (see Fig. 3).

waves propagate eastward with periods near 20 days (Randel and Wu 2005; Flannaghan and Fueglistaler 2013; Scherrlin-Pirscher et al. 2017; Kim et al. 2019) in contrast to the quasi-stationary patterns seen here (section 4).

d. Links with deep convection

This section explores the relationships between the occurrence of inversions and deep convection, based on OLR as a proxy for convection. Figure 12 shows the longitude-versus-time distribution of OLR over the equator for the summer of 2009, highlighting episodic low values (enhanced convection) occurring close in time with temperature inversions at 15 km (black contours in Fig. 12). Enhanced convection occurs nearby or somewhat to the east of the strongest inversions. Space-based lidar observations (browse images from https://www-calipso.larc.nasa.gov/products/) show that the associated convective clouds reach to near the tropopause level (~16 km) for each of the large-scale events in Fig. 12.

Composite analysis of OLR anomalies for episodes of enhanced Indian monsoon inversions at 15 km were generated as discussed above, including analyzing time-lag behavior. Time-lag evolution of the composited OLR

variations over the equator (Fig. 13a) shows the strongest signal occurs for convection leading the inversions by ~2–6 days, which is strong evidence that convection is a key forcing mechanism for forming the inversions. Figure 13b shows the composite OLR anomalies leading the inversions by 2–6 days; these are the lag times with the strongest OLR signal. Results show a strong negative OLR anomaly (enhanced convection) over the equatorial Indian Ocean, with a similar pattern to the inversion occurrence frequency map in Fig. 3.

The patterns in Figs. 13a and 13b show that enhancements in convection over the Indian Ocean occur in concert with decreases nearby and east of the Philippines (red colors in Figs. 13a and 13b), so this represents an east–west seesaw in convection tied to the upper-level inversions. This behavior is similar to patterns of intraseasonal OLR variability in the Indian monsoon identified by Lau and Chan (1986) and Annamalai and Slingo (2001).

The link between convection and temperatures/winds can also be analyzed based on composites with respect to the strongest convection over the equatorial Indian Ocean (region highlighted in Fig. 13a). This analysis is a complement to the composites based on inversion frequency. We perform composites based on daily average OLR time series, and select time periods with strongest
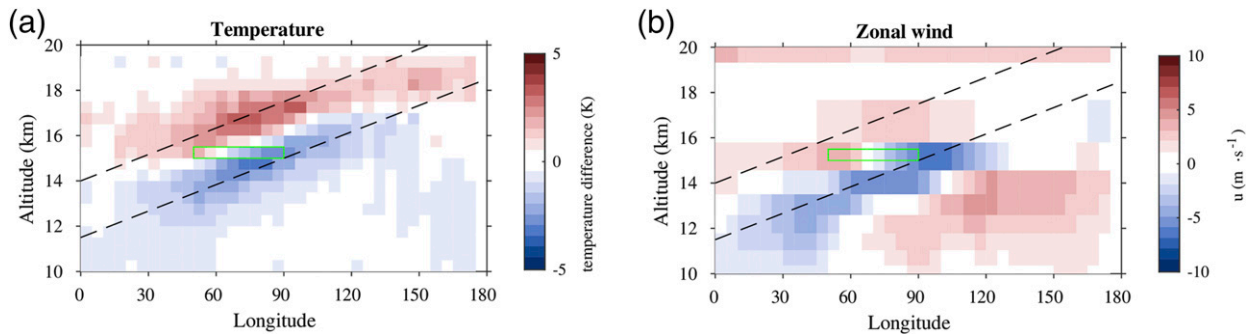
FIG. 10. (a) Temperature and (b) zonal wind anomalies over the equator for composites of high-frequency vs low-frequency inversion events at 15 km in the Indian monsoon. The dashed lines help identify the phase structure between temperature and zonal wind, which correspond to a vertical wavelength of ~5 km.

anomalies (strong convection defined as $OLR < 225\,W\,m^{-2}$, weak/no convection defined as $OLR > 260\,W\,m^{-2}$). The horizontal and vertical structure of temperature and wind anomalies linked to strong convection over the Indian Ocean (Fig. 14) have the same characteristics as those deduced for frequent inversions (Figs. 10 and 11). The links to transient equatorial deep convection are consistent with a convectively forced equatorial Kelvin wave (e.g., Garcia and Salby 1987). This is similar to the behavior highlighted by Nishimoto and Shiotani (2012), who noted a temperature anomaly in a "horseshoe shape" to the east, centered on the equator, as a response to deep convection in this region during boreal summer. Temporal variation of the 16 km temperature response to convection (Fig. 15) highlight that largest anomalies occur a few days after the strongest convection, with patterns that are quasi stationary and slowly eastward moving with time.

4. Quasi-stationary Kelvin waves

The upper-tropospheric anomalies linked with inversions and their relationships with convection have

characteristics of large-scale Kelvin waves, including equatorially centered coherent temperature and wind anomalies with an eastward phase tilt with height and a vertical wavelength around 5 km. Furthermore, the evidence indicates that the waves are forced by transient deep convection near the equator, consistent with convectively forced, equatorially trapped Kelvin waves (e.g., Garcia and Salby 1987). However, Kelvin waves in the upper troposphere and lower stratosphere typically propagate eastward (e.g., Randel and Wu 2005; Flannaghan and Fueglistaler 2011; Scherllin-Pirscher et al. 2017), so the quasi-stationary behavior here seems anomalous. However, this may be explained by the strong background easterly winds in the region as a part of the Indian monsoon anticyclone.

The intrinsic zonal phase velocity c_{int} for Kelvin waves is given by

$$c_{int} = \frac{N\lambda_z}{2\pi}, \qquad (2)$$

[Andrews et al. 1987, their Eq. (4.7.8)], where N is the Brunt–Väisälä frequency (~$0.01\,s^{-1}$ for the troposphere, ~$0.02\,s^{-1}$ for the stratosphere), and λ_z is the vertical wavelength of the waves, which can be estimated from
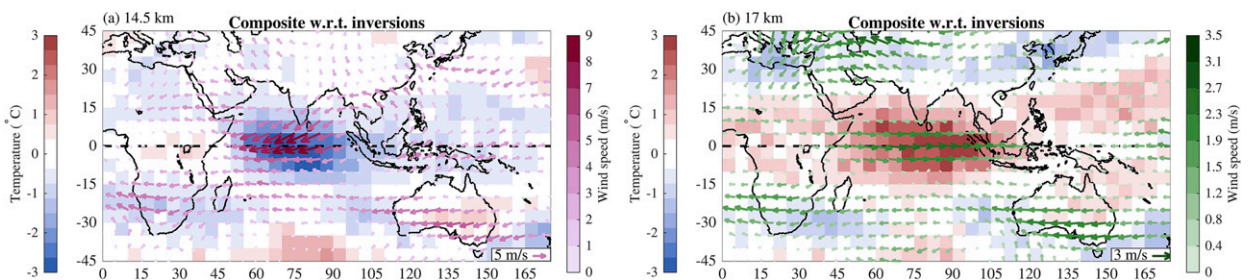

FIG. 11. Composite temperature (shading) and wind (arrows) anomalies for high-frequency vs low-frequency inversion events over the equatorial Indian Ocean. Horizontal structure at (a) 14 and (b) 17 km. These two levels are shown as they correspond to the positive and negative anomaly amplitudes of the wave (Fig. 10). The wind vectors are colored and scaled by wind speed, with reference vectors in the bottom right of each plot.
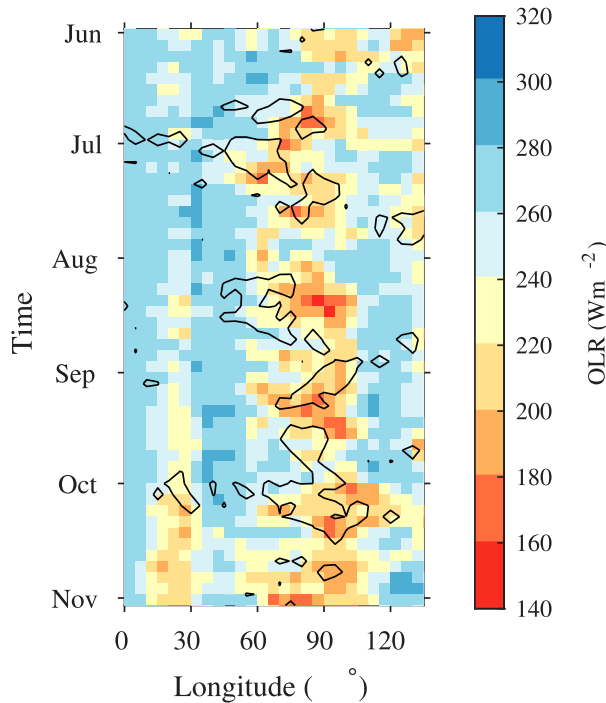
FIG. 12. Longitude–time plot of outgoing longwave radiation (OLR) over the equator during summer 2009. Orange and red colors denote enhanced deep convection. The black contours enclose areas that have >30% of profiles with temperature inversions at 15 km (see Fig. 3).

Fig. 10a to be ~5 km, so the phase velocity, relative to the surrounding air, is $c \approx 8 \, \text{m s}^{-1}$ (tropospheric N) to $\approx 16 \, \text{m s}^{-1}$ (stratospheric N). This phase velocity is similar (with opposite sign) to the near-equatorial easterly zonal winds of ~10–20 m s^{-1} in this region, as illustrated

in Fig. 16. Therefore, the zonal phase velocity relative to the ground, $c_{\text{gmd}} = c_{\text{int}} + u$, where u is the background zonal wind, is approximately zero.

Although the substantial wind shear (and change in N across the tropopause) precludes a simple evaluation of a Doppler-shifted Kelvin wave phase speed, the approximate agreement between the calculated phase speed and background winds, along with their coincidence in space and time over the Indian Ocean during boreal summer, is strong evidence for this mechanism to explain a quasi-stationary Kelvin wave behavior. Similar calculations of the latitudinal e-folding distance for a Kelvin wave with a vertical wavelength of 5 km [Andrews et al. 1987, their Eq. (4.7.9)] gives a value of ~10° of latitude, which is consistent with the latitudinal width of the temperature and wind anomalies (Fig. 11). Because the inversions are primarily observed over the equatorial Indian Ocean during boreal summer, it is theorized that they exist here as a result of local episodic convection that initiates wave activity, the proximity to the equator, which acts as the waveguide for the Kelvin waves, and the strong easterly winds to the south of the monsoon anticyclone that Doppler shifts the eastward propagating Kelvin waves and sustain their quasi-stationary nature. This explanation is similar to that proposed by Nishi et al. (2010).

5. Summary and discussion

A climatology of upper-tropospheric temperature inversions shows the most frequent inversions occur over the equatorial Indian Ocean during the months of July–September. The inversions are found inclined
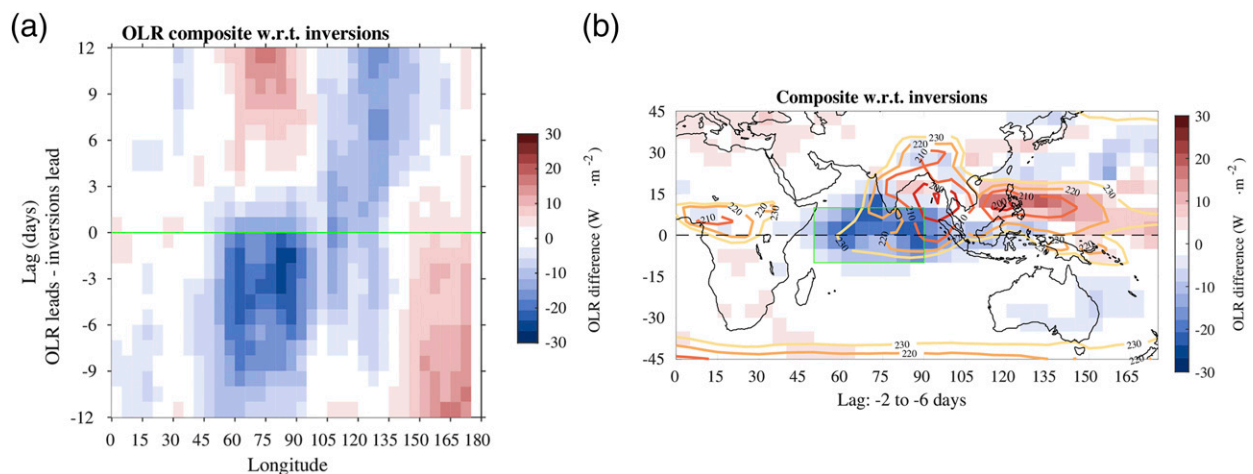

FIG. 13. Composite OLR anomalies between high-frequency vs low-frequency inversion events in the Indian monsoon. (a) Time-lag evolution over the equator and (b) spatial structure of OLR anomalies. Blue regions indicate increased convection (lower OLR) associated with higher inversion percentages at 15 km. The maximum at negative time lags in (a) denotes that deep convection precedes the upper-tropospheric inversions. Also plotted in (b) is the climatological mean OLR (colored contour lines).
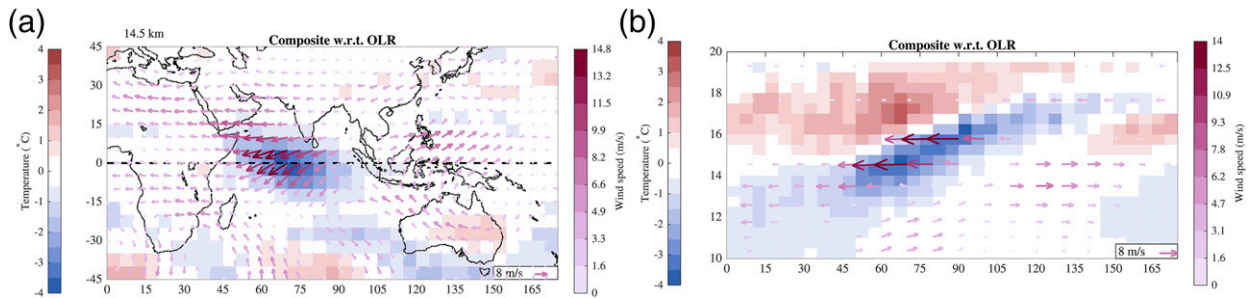
FIG. 14. Composite temperature and wind anomalies for strong vs weak convective events over the equatorial Indian Ocean (box indicated in Fig. 13). (a) Horizontal structure at 14.5 km and (b) height vs longitude at 0°.

from the horizontal plane: on the eastern side of the region the inversions are at 15–16 km and are strongest and most frequently observed, while inversions to the west are found around 13–14 km and are weaker. Strong inversions can lower the local LRT by ∼1 km compared to the background, and this accounts for the localized climatological minimum in LRT in this region (Schmidt et al. 2005; Munchak and Pan 2014). The inversions occur episodically several times each year, with a time scale of 1–2 weeks, as first identified by Nishi et al. (2010). The inversions are linked to large-scale temperature and wind anomalies in the upper troposphere–lower stratosphere (UTLS), with convective forcing in the equatorial Indian Ocean preceding the inversions by ∼2–6 days (Fig. 13). Large-scale temperature and wind anomalies in the UTLS occur consistent with an equatorially centered Kelvin wave, with a characteristic eastward tilt with height. The upper-tropospheric wind anomalies are substantial (∼10 m s^{-1}), and strongly modulate the background equatorial easterly winds as part of the Indian monsoon anticyclone (Figs. 11a and 16). The calculated intrinsic eastward zonal phase speed for $\lambda_z \sim 5$ km Kelvin waves in the UTLS is ∼8–16 m s^{-1}, and Doppler shifting by the background easterly winds (Fig. 16) can explain the quasi-stationary nature of the apparent Kelvin wave response. The confluence of near-equatorial convective forcing with strong localized easterly background winds is a unique situation, which can explain the regular seasonal occurrence of the large-scale waves and upper-tropospheric inversions.

Lag correlations clearly demonstrate that enhanced equatorial convection precedes the inversion events by several days (Fig. 13), but the strong quasi-stationary temperature response in the upper troposphere could potentially feed back onto the large-scale convective structure in this region. In particular, the large-scale cold anomalies over ∼12–15 km will decrease the static stability over the top of the convective region (as shown schematically in Fig. 16), possibly allowing for enhanced

or prolonged convective organization or phase locking with the upper level circulation (anchoring) in this region. This is a complex feedback that could be explored in idealized numerical simulations.

Another aspect of interest could be the relationship of the quasi-stationary Kelvin waves to atmospheric turbulence. Fujiwara et al. (2003b) document enhanced UTLS turbulence tied to breaking equatorial Kelvin waves, and Flannaghan and Fueglistaler (2011) note the relationship of shear–flow instability and Kelvin waves in the UTLS diagnosed from reanalysis data. A recent diagnosis of the thermodynamic budget from reanalyses (Tegtmeier et al. 2020, their Fig. S8.8.4, manuscript submitted to SPARC Reanalysis Intercomparison Project Rep.) shows a relatively strong contribution to parameterized diffusive heat transport over the Indian Ocean during boreal summer, possibly linked to the quasi-stationary Kelvin waves studied here. Note that the Kelvin waves enhance the strong background zonal wind shears in the UTLS (Fig. 16), providing a mechanism
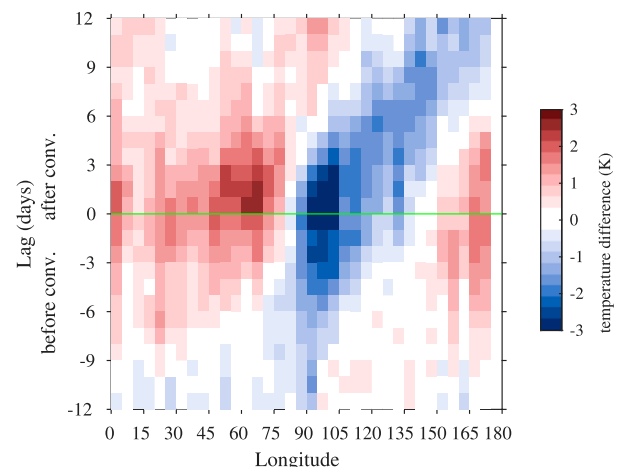

FIG. 15. Time-lag variations of equatorial temperature at 16 km composited for enhanced convection over the equatorial Indian Ocean (region highlighted in Fig. 13).
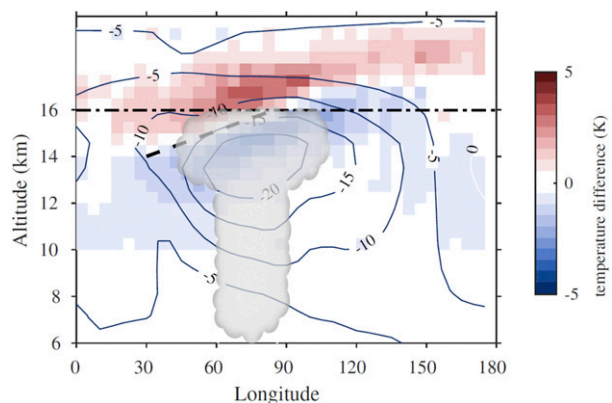
FIG. 16. Schematic diagram of the important contributing factors to the inversions, including the composite temperature anomalies for high-frequency vs low-frequency inversion events (shaded), the average background zonal winds from 10°S to 10°N (line contours), and convection that reaches ~16 km (cloud image). Also plotted is the climatological tropopause near 16 km (dash–dotted line), and the location of the high inversion percentages (dashed line).

for episodic shear-induced turbulence tied to the inversions. Exploring this behavior may be a fruitful avenue for further investigation.

REFERENCES

Andrews, D. G., J. R. Holton, and C. B. Leovy, 1987: *Middle Atmosphere Dynamics*. International Geophysics Series, Vol. 40, Academic Press, 489 pp.

Annamalai, H., and J. Slingo, 2001: Active/break cycles: Diagnosis of the intraseasonal variability of the Asian summer monsoon. *Climate Dyn.*, **18**, 85–102, https://doi.org/10.1007/s003820100161.

Anthes, R. A., and Coauthors, 2008: The COSMIC/FORMOSAT-3 mission: Early results. *Bull. Amer. Meteor. Soc.*, **89**, 313–334, https://doi.org/10.1175/BAMS-89-3-313.

Beyerle, G., T. Schmidt, G. Michalak, S. Heise, J. Wickert, and C. Reigber, 2005: GPS radio occultation with GRACE: Atmospheric profiling utilizing the zero difference technique.

Geophys. Res. Lett., **32**, L13806, https://doi.org/10.1029/2005GL023109.

——, and Coauthors, 2011: First results from the GPS atmosphere sounding experiment TOR aboard the TerraSAR-X satellite. *Atmos. Chem. Phys.*, **11**, 6687–6699, https://doi.org/10.5194/ACP-11-6687-2011.

Biondi, R., W. J. Randel, S.-P. Ho, T. Neubert, and S. Syndergaard, 2012: Thermal structure of intense convective clouds derived from GPS radio occultations. *Atmos. Chem. Phys.*, **12**, 5309–5318, https://doi.org/10.5194/acp-12-5309-2012.

——, S.-P. Ho, W. J. Randel, S. Syndergaard, and T. Neubert, 2013: Tropical cyclone cloud-top height and vertical temperature structure detection using GPS radio occultation measurements. *J. Geophys. Res. Atmos.*, **118**, 5247–5259, https://doi.org/10.1002/JGRD.50448.

Dee, D. P., and Coauthors, 2011: The ERA-Interim reanalysis: Configuration and performance of the data assimilation system. *Quart. J. Roy. Meteor. Soc.*, **137**, 553–597, https://doi.org/10.1002/qj.828.

Flannaghan, T. J., and S. Fueglistaler, 2011: Kelvin waves and shear-flow turbulent mixing in the TTL in (re-)analysis data. *Geophys. Res. Lett.*, **38**, L02801, https://doi.org/10.1029/2010GL045524.

——, and ——, 2013: The importance of the tropical tropopause layer for equatorial Kelvin wave propagation. *J. Geophys. Res. Atmos.*, **118**, 5160–5175, https://doi.org/10.1002/JGRD.50418.

Fujiwara, M., S.-P. Xie, M. Shiotani, H. Hashizume, F. Hasebe, H. Vömel, S. J. Oltmans, and T. Watanabe, 2003a: Upper-tropospheric inversion and easterly jet in the tropics. *J. Geophys. Res.*, **108**, 4796, https://doi.org/10.1029/2003JD003928.

——, M. K. Yamamoto, H. Hashiguchi, T. Horinouchi, and S. Fukao, 2003b: Turbulence at the tropopause due to breaking Kelvin waves observed by the Equatorial Atmosphere Radar. *Geophys. Res. Lett.*, **30**, 1171, https://doi.org/10.1029/2002GL016278.

Garcia, R. R., and M. L. Salby, 1987: Transient response to localized episodic heating in the tropics. Part II: Far-field behavior. *J. Atmos. Sci.*, **44**, 499–532, https://doi.org/10.1175/1520-0469(1987)044<0499:TRTLEH>2.0.CO;2.

Hajj, G. A., and Coauthors, 2004: CHAMP and SAC-C atmospheric occultation results and intercomparisons. *J. Geophys. Res.*, **109**, D06109, https://doi.org/10.1029/2003JD003909.

Hoskins, B. J., and M. J. Rodwell, 1995: A model of the Asian summer monsoon. Part I: The global scale. *J. Atmos. Sci.*, **52**, 1329–1340, https://doi.org/10.1175/1520-0469(1995)052<1329:AMOTAS>2.0.CO;2.

Johnson, R. H., P. E. Ciesielski, and K. A. Hart, 1996: Tropical inversions near the 0°C level. *J. Atmos. Sci.*, **53**, 1838–1855, https://doi.org/10.1175/1520-0469(1996)053<1838:TINTL>2.0.CO;2.

Kim, Y.-H., and Coauthors, 2019: Comparison of equatorial wave activity in the tropical tropopause layer and stratosphere represented in reanalyses. *Atmos. Chem. Phys.*, **19**, 10 027–10 050, https://doi.org/10.5194/acp-19-10027-2019.

Lau, K.-M., and P. H. Chan, 1986: Aspects of the 40–50 day oscillation during the northern summer as inferred from outgoing longwave radiation. *Mon. Wea. Rev.*, **114**, 1354–1367, https://doi.org/10.1175/1520-0493(1986)114<1354:AOTDOD>2.0.CO;2.

Liebmann, B., and C. A. Smith, 1996: Description of a complete (interpolated) outgoing longwave radiation dataset. *Bull. Amer. Meteor. Soc.*, **77**, 1275–1277, https://doi.org/10.1175/1520-0477-77.6.1274.

Mapes, B. E., and P. Zuidema, 1996: Radiative–dynamical consequences of dry tongues in the tropical troposphere. *J. Atmos.*

Sci., **53**, 620–638, https://doi.org/10.1175/1520-0469(1996)053<0620:RDCODT>2.0.CO;2.

Munchak, L. A., and L. L. Pan, 2014: Separation of the lapse rate and the cold point tropopauses in the tropics and the resulting impact on cloud top-tropopause relationships. *J. Geophys. Res. Atmos.*, **119**, 7963–7978, https://doi.org/10.1002/2013JD021189.

Newell, R. E., V. Thouret, J. Y. N. Cho, P. Stoller, A. Marenco, and H. G. Smit, 1999: Ubiquity of quasi-horizontal layers in the troposphere. *Nature*, **398**, 316–319, https://doi.org/10.1038/18642.

Nishi, N., E. Nishimoto, H. Hayashi, M. Shiotani, H. Takashima, and T. Tsuda, 2010: Quasi-stationary temperature structure in the upper troposphere over the tropical Indian Ocean inferred from radio occultation data. *J. Geophys. Res.*, **115**, D14112, https://doi.org/10.1029/2009JD012857.

Nishimoto, E., and M. Shiotani, 2012: Seasonal and interannual variability in the temperature structure around the tropical tropopause and its relationship with convective activities. *J. Geophys. Res.*, **117**, D02104, https://doi.org/10.1029/2011JD016936.

Randel, W. J., and F. Wu, 2005: Kelvin wave variability near the equatorial tropopause observed in GPS radio occultation measurements. *J. Geophys. Res.*, **110**, D03102, https://doi.org/10.1029/2004JD005006.

——, D. J. Seidel, and L. L. Pan, 2007: Observational characteristics of double tropopauses. *J. Geophys. Res.*, **112**, D07309, https://doi.org/10.1029/2006JD007904.

Scherllin-Pirscher, B., W. J. Randel, and J. Kim, 2017: Tropical temperature variability and Kelvin-wave activity in the UTLS from GPS RO measurements. *Atmos. Chem. Phys.*, **17**, 793–806, https://doi.org/10.5194/acp-17-793-2017.

Schmidt, T., S. Heise, J. Wickert, G. Beyerle, and C. Reigber, 2005: GPS radio occultation with CHAMP and SAC-C: Global monitoring of thermal tropopause parameters. *Atmos. Chem. Phys.*, **5**, 1473–1488, https://doi.org/10.5194/acp-5-1473-2005.

von Engeln, A., Y. Andres, C. Marquardt, and F. Sancho, 2011: GRAS radio occultation on-board of MetOp. *Adv. Space Res.*, **47**, 336–347, https://doi.org/10.1016/J.ASR.2010.07.028.

Wallace, J. M., and V. E. Kousky, 1968: Observational evidence of Kelvin waves in the tropical stratosphere. *J. Atmos. Sci.*, **25**, 900–907, https://doi.org/10.1175/1520-0469(1968)025<0900:OEOKWI>2.0.CO;2.

Wickert, J., and Coauthors, 2001: Atmosphere sounding by GPS radio occultation: First results from CHAMP. *Geophys. Res. Lett.*, **28**, 3263–3266, https://doi.org/10.1029/2001GL013117.